Pergamon

Int. J. Heat Mass Transfer. Vol. 39, No. 17, pp. 3633–3647, 1996

0017–9310/96 $15.00 + 0.00

PII: S0017–9310(96)00035–X

Numerical study of a low permeability microporous heat sink for cooling phased-array radar systems

J. L. LAGE and A. K. WEINERT
Mechanical Engineering Department, Southern Methodist University, Dallas, TX 75275-0337, U.S.A.

D. C. PRICE
Aero-Thermal Technology Branch, Defense Systems and Electronics Group, Texas Instruments, Plano, TX 75086-9305, U.S.A.

and

R. M. WEBER
Advanced Programs Division, Defense Systems and Electronics Group, Texas Instruments, Plano, TX 75086-9305, U.S.A.

(*Received* 12 *July* 1995 *and in final form* 19 *January* 1996)

Abstract—Microporous media is being used to develop an improved forced convection cold plate device for removing waste heat from high frequency phased-array radar apertures. The waste heat, generated by transmit and receive microwave functions mounted in separate electronic modules, is conducted to the surfaces of a thin rectangular enclosure (cold plate) through which coolant flows. The performance of the phased-array radar is known to deteriorate very rapidly when the difference in operating temperatures of identical electronic components within each module increases. The cold plate device investigated here, designed to minimize this temperature difference, consists of a microporous layer placed (brazed) within the cold plate. A theoretical transport model is developed around an extended system of two-dimensional equations obtained by considering a thin enclosure and integrating the original three-dimensional equations along the direction of smaller dimension. Thermo/hydraulic characteristics are obtained through numerical simulations considering a low permeability aluminum alloy porous layer, and air, water and PAO as coolants. A theoretical estimate of the global pressure drop across the cold plate is also obtained and compared with the numerical results. The microporous cold plate provides substantially more uniform operating temperature for identical components in all module housings than a cold plate without porous layer. Results also suggest an increased global heat transfer coefficient reducing the operational (junction) temperature of the electronics for the same waste heat. Copyright © 1996 Elsevier Science Ltd.

BACKGROUND

Existing techniques for cooling electronics were recently reviewed by Mudawar *et al.* [1], including: passive natural convection, forced convection cooling (falling films, jet impingement), sub-cooled liquid immersion cooling, and cooling by change of phase (pool boiling, flow boiling). All these alternatives are implemented in unobstructed channels. Heat dissipated by the electronic components is typically transferred by conduction to the surfaces of a cooling channel and then convected away by the coolant. The heat transfer area is fixed by the surface area of the cooling enclosure.

Another cooling strategy is the use of microchannel heat sinks. A very interesting review of the subject was provided by Walpole and Missaggia [2]. Microchannel heat sinks are considered a promising technological alternative for cooling high-power density electronic packages. A practical application of microchannel heat sinks is found in cooling diode laser arrays. These heat sinks are normally built by etching regular microchannels (typically 100 μm wide by 200 μm high) in a silicon wafer. The wafer is then soldered to the diode laser array slat surface and against a cover plate. The solid region of the wafer, seen as microfins, presents a much larger heat transfer surface area increasing the thermal efficiency of the cooling enclosure. Typical microchannel heat sinks operate between 70 and 700 kPa of pressure drop from 5×10^{-6} to 30×10^{-6} m^3 s^{-1} of cooling water. The maximum thermal resistance is about 10^{-5} m^2°C W^{-1} for 5 kW m^{-2} of power dissipated within a 4×10^{-6} m^2 surface area [2]. Recent experimental work by Peng *et al.* [3] indicated that flat-plate rectangular microchannels are capable of dissipating in excess of 10

NOMENCLATURE

c_p	specific heat [J kg^{-1} K^{-1}]
c_F	Forchheimer coefficient
Da	Darcy number
e	inlet and outlet depth [m]
$f, F, F^{(2)}$	shape factors, equation (9)
g	shape function, equation (4)
h	enclosure height [m]
H	nondimensional enclosure height
J	effective viscosity coefficient
k	thermal conductivity [W m^{-2} K^{-1}]
K	permeability [m^2]
p	pressure [Pa]
P	nondimensional pressure
Pr	Prandtl number
q	heat transfer [W]
r	enclosure width [m]
R	nondimensional enclosure width
Re	Reynolds number
s	enclosure depth [m]
S	nondimensional enclosure depth
T	temperature [K]
u, v, w	Cartesian fluid (seepage) velocity components [m s^{-1}]
U, V	nondimensional velocity components
x, y, z	Cartesian coordinates [m]
X, Y	nondimensional Cartesian coordinates.

Greek symbols

α	thermal diffusivity [m^2 s^{-1}]
β	auxiliary parameter, equation (14)
ε	relative porous layer volume
ϕ	porosity
ν	kinematic viscosity [m^2 s^{-1}]
θ	nondimensional temperature
Γ	auxiliary parameter, equation (14)
ρ	density [kg m^{-3}].

Superscripts

$( )'''$	per unit of volume
$( )''$	per unit of area
$( )'$	two dimensional
$( )^*$	effective
$\overline{( )}$	surface averaged.

Subscripts

b	bottom
f	nonporous (fluid)
h	heating
H	Hsu *et al.*'s [16] model
m	porous (fluid and solid matrix)
s	solid
t	top
in	inlet
out	outlet.

kW m^{-2} with single phase convective cooling, using methanol as coolant.

It is interesting to note that by etching interrupted microchannels (alternate flow channels), the maximum temperature of the electronics is reduced for the same coolant flow rate and same dissipating heat. This is a consequence of the better mixing provided by the irregular channels. If the channels are built with irregularities that are randomly oriented, the solid structure will become, eventually, porous-isotropic. A natural extension would be a *microporous heat sink* as the one studied here. Although porous media is well known for enhancing the heat transfer capabilities of thermal systems (e.g. refs. [4–6]), the practical implications of using it to improve the removal of microelectronics waste heat is yet to be investigated [7].

Most of the existing research on cooling electronics has been geared towards finding an effective cooling technique to maintain the junction temperature of the components within acceptable limits. The development of some advanced microelectronics systems faces a more challenging cooling restriction. Typical examples are high frequency phased-array radar systems. These arrays, now in development by Texas Instruments, can dissipate in excess of 20 kW m^{-2}. The temperature of the electronics in these systems is maintained within acceptable limits by removing the dissipated heat via the component mounting surfaces of a cold plate. Coolant circulates within the cold plate transporting the waste heat to an environmental control unit. An extra requirement, from a system operational view, is to minimize temperature gradients between identical components in each transmit and receive microwave housing module. This is a fundamental requirement to improve the overall performance of the system.

PHASED-ARRAY RADAR

Figure 1(A) presents a schematic of a typical phased-array radar slat. All the modules of a phased-array radar are mounted in the same plane, all are oriented in the same direction, and are steered electronically as controlled by computer. A classical, old-style, radar would consist of an antenna that would be mechanically moved or rotated in azimuth and elevation to *look* in all directions. A phased-array radar remains fixed and is electronically steered to *look* in all directions.

The modules of a phased-array, R_f amplifiers made of gallium arsenide (GaAs) integrated circuits on thin film ceramic substrates, are temperature sensitive. If two modules are maintained at different temperatures,

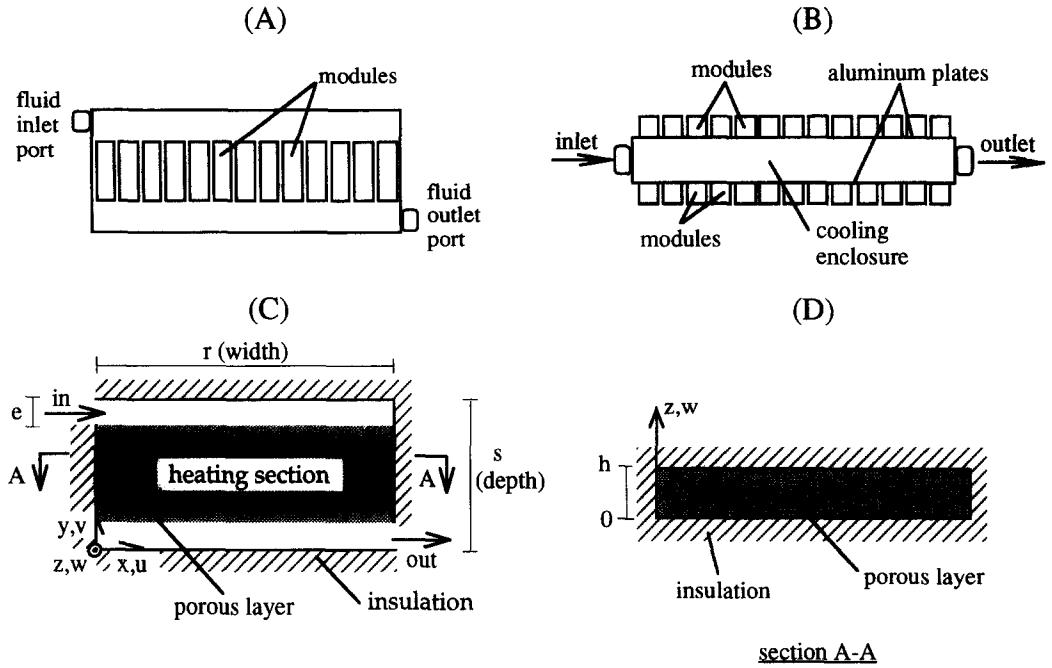

Fig. 1. Phased-array radar electronic slat (A), with modules attached to cold plate surfaces (B), model representation of the physical system (C), with porous layer sandwiched between aluminum plates (D).

the *phase-shifters* will cause them to *look* in different directions. This directional error is called a *phase-shift* error. The thermal challenge is to ensure that identical components within each module are cooled to near identical temperatures. The larger the temperature differences between modules, the larger the phase-shift error.

The modules are conductively coupled at the base to a liquid-cooled enclosure or cold plate [Fig. 1(B)]. The power dissipated by the components is transferred through aluminum plates to the coolant that flows through the enclosure. The difficulty in obtaining uniform temperature from module to module is caused primarily by nonuniform flow distribution within the cooling enclosure.

Figure 1, (C, D), show a model representation of the cold plate design developed jointly by Southern Methodist University and Texas Instruments. The main feature of this design is a porous layer placed within the enclosure, sandwiched between the top and bottom aluminum plates. A strong candidate for porous material being investigated is a 6101-T6 aluminum alloy porous foam. The foam can be vacuum brazed with the interior surfaces of the cold plate enclosure, therefore providing minimal contact thermal resistance and structural rigidity.

A cold plate without a porous layer in it is referred to as a *nonporous* or *clear* configuration. In this case, with no obstruction to the flow path, the coolant will flow from inlet to outlet in a *diagonal flow* configuration. A porous layer, placed within the cooling enclosure, is expected to induce the alignment of the flow with the y-axis parallel to the microwave modules, in a *parallel flow* configuration. In this case, the cold plate heating section [Fig. 1, (C)] is expected to be cooled uniformly along the transversal (x) direction.

MATHEMATICAL MODEL

Consider the flow of incompressible Newtonian field with constant properties through a heterogeneous system [Fig. 1, (C)]. The fluid saturates the rigid, homogeneous and isotropic porous matrix. The fluid and solid matrix are supposed to be in thermal equilibrium. The steady-state three-dimensional equations of mass, momentum and energy balance are [8], respectively,

$$\nabla \cdot \mathbf{W} = 0, \tag{1}$$

$$\frac{1}{\phi^2}(\mathbf{W}\nabla)\cdot\mathbf{W} = -\frac{1}{\phi\rho}\nabla p + Jv\nabla^2\mathbf{W} - \frac{v}{K}\mathbf{W} - \frac{c_F}{K^{1/2}}|\mathbf{W}|\mathbf{W}, \tag{2}$$

$$\mathbf{W}\cdot\nabla T = \frac{k_m}{\rho c_p}\nabla^2 T + \frac{1}{\rho c_p}q''', \tag{3}$$

where $\mathbf{W}$ is local fluid (seepage) velocity vector, $\mathbf{W} = u\mathbf{i} + v\mathbf{j} + w\mathbf{k}$, p is pressure, T is temperature. Fluid quantities are the density, ρ, specific heat, c_p and kinematic viscosity, v. Saturated porous medium quantities are the effective thermal conductivity, k_m, porosity, ϕ, effective viscosity coefficient, J, permeability, K, and Forchheimer inertia coefficient, c_F. Other parameters of interest are the height, h, depth, s, and width, r, of the enclosure [Fig. 1, (C, D)].

The macroscopic flow shear effect within the porous medium, accounted for by the Brinkman term (Laplacian term), is written with an effective viscosity coefficient, J. This coefficient is the ratio between the effective (porous) kinematic viscosity (ν_m) and the fluid kinematic viscosity, $J = \nu_m/\nu$. For a low permeability porous medium, this factor can be set equal to $1/\phi$ [9]. Notice that when $\phi = 1$ and $K \to \infty$, equation (2) takes the form of the Navier–Stokes equation, accurate for modeling flow through a nonporous region.

The energy equation (3) reveals the uniform volumetric heating model adopted here. This model is expected to be reasonably accurate when modeling heat transfer through thin enclosures. Notice that arrays designed by Texas Instruments present identical top and bottom modules, in which case the same heat dissipated at the top will be dissipated also on the bottom. The volumetric heat parameter of the rightmost term, q''', represents the total power generated by the top and bottom electronic components per unit of volume, $q''' = (q_t'' + q_b'')/h = q''/h$. This volumetric heat source is considered only within the region sandwiched by the two layers of electronic components (heating region), being zero everywhere else within the enclosure (the spacing in-between modules, shown in Fig. 1, (A, and B), is for clarity only—in practice the module housings are placed in contact with each other, therefore the heating region is essentially a continuous region along the x-direction). Notice also that by replacing the effective thermal conductivity by the fluid thermal conductivity, equation (3) becomes valid for a nonporous region. As secondary dispersion effects within the porous layer are not accounted for, the cooling effect obtained by solving the system of equations (1)–(3) is conservative.

Considering a slender enclosure, $h \ll (r, s)$, the vertical (z) variation of pressure can be neglected. The velocity field is then assumed to be fully developed in z within both, nonporous and porous, regions. The horizontal velocity components can be written as the product of the h-averaged horizontal velocity components, u' and v', with a shape function that determines the velocity profile in the z-direction, $g(z)$,

$$p(x,y,z) = p'(x,y), \quad u(x,y,z) = u'(x,y)g_{f,m}(z),$$
$$v(x,y,z) = v'(x,y)g_{f,m}(z), \quad w(x,y,z) = 0. \tag{4}$$

The double subscript in shape function g (m for porous region and f for nonporous region) anticipates different velocity profiles within each region. The temperature is also considered to have negligible variation in the z-direction,

$$T(x,y,z) = T'(x,y). \tag{5}$$

With equations (4) and (5), the three-dimensional balance equations (1)–(3) can be integrated in z, from zero to h. The resulting equations, valid for a slender cooling enclosure, are

$$\nabla \cdot \mathbf{W}' = 0 \tag{6}$$

$$\frac{F_{f,m}^{(2)}}{\phi^2}(\mathbf{W}'\nabla)\cdot\mathbf{W}' = -\frac{1}{\phi\rho}\nabla p' + F_{f,m}J\nu\nabla^2\mathbf{W}' - \left(-\frac{J2f_{f,m}}{h^2} + \frac{F_m}{K}\right)\nu\mathbf{W}' - \frac{F_m^{(2)}c_F}{K^{1/2}}|\mathbf{W}'|\mathbf{W}' \tag{7}$$

$$\mathbf{W}'\cdot\nabla T' = \frac{1}{F_{f,m}}\frac{k_m}{\rho c_p}\nabla^2 T' + \frac{1}{F_{f,m}}\frac{1}{\rho c_p h}q'', \tag{8}$$

where

$$F_{f,m} = \frac{1}{h}\int_0^h g_{f,m}\,dz, \quad F_{f,m}^{(2)} = \frac{1}{h}\int_0^h g_{f,m}^2\,dz$$
$$\text{and} \quad f_{f,m} = h\left.\frac{dg_{f,m}}{dz}\right|_h. \tag{9}$$

Notice that $F_{f,m}$ is identically equal to one because $\mathbf{W}'$ is the z-averaged velocity (recall that $\mathbf{W}' = u'\mathbf{i} + v'\mathbf{j}$). Once the shape functions for the nonporous and porous regions are known and the nondimensional shape factors, $F_{f,m}^{(2)}$ and $f_{f,m}$, computed, equations (6)–(8) will form a system of two-dimensional nonlinear partial differential equations. The dimensional simplification from three to two dimensions, although straightforward, requires the additional effort of determining the nondimensional shape factors listed in equation (9).

The system of equations (6)–(8) is nondimensionalized with the following group of dimensionless parameters: $(X, Y) = (x, y)/e$, $\mathbf{V} = (1/u_{in})\mathbf{W}'$, $P = p'/(\rho u_{in}^2)$, $\theta = (T' - T_{in})/(q''h/k_m)$, $H = h/e$, $Re = u_{in}e/\nu$, $Da = K/e^2$, $Pr_m = \nu/\alpha_m$, $\alpha_m = k_m/(\rho c_p)$, where e is the depth of the inlet and outlet ports [Fig. 1, (C)]. The nondimensional system is

$$\nabla \cdot \mathbf{V} = 0, \tag{10}$$

$$(\mathbf{V}\nabla)\cdot\mathbf{V} = -\frac{\phi}{F_{f,m}^{(2)}}\nabla P + \frac{\phi^2 J}{F_{f,m}^{(2)}Re}\nabla^2\mathbf{V} - \left(-\frac{J2f_{f,m}}{H^2F_{f,m}^{(2)}} + \frac{1}{F_m^{(2)}Da}\right)\frac{\phi^2}{Re}\mathbf{V} - \frac{c_F\phi^2}{Da^{1/2}}|\mathbf{V}|\mathbf{V}, \tag{11}$$

$$\mathbf{V}\cdot\nabla\theta = \frac{1}{Pr_m Re}\nabla^2\theta + \frac{1}{H^2 Pr_m Re}. \tag{12}$$

Notice that (X, Y), $\mathbf{V}(= U\mathbf{i} + V\mathbf{j})$, P and θ are, respectively, horizontal coordinates, horizontal fluid velocity vector, pressure and temperature. Additional nondimensional groups in equations (10)–(12) are the height, H, the Reynolds number, Re, the Darcy number, Da, and the porous modified Prandtl number, Pr_m.

Nondimensional boundary conditions are impermeable, nonslip, and adiabatic solid surfaces ($U = V = \partial\theta/\partial X = \partial\theta/\partial Y = 0$), uniform and iso-

thermal inlet flow ($U = 1$ and $V = \theta = 0$), and non-diffusion outlet boundary ($\partial U/\partial X = \partial\theta/\partial X = 0$).

SHAPE FACTORS

Attention is now turned to evaluating the $F^{(2)}_{f,m}$ and $f_{f,m}$ terms. Within a nonporous region, the fully developed velocity profile is represented by $g_f(z) = 6z(h-z)/h^2$, so

$$F^{(2)}_f = \frac{6}{5} \quad \text{and} \quad f_f = -6. \tag{13}$$

The situation is more complex when considering the flow within a porous medium region. Unfortunately, a unique closed form solution valid for all ranges of Da and c_F does not exist, so it is necessary to proceed on a case-by-case basis. For a low permeability matrix as considered here, low enough to validate a Brinkman-extended Darcy model (in a scaling form, $Da \ll 1/(\phi Re c_F)^{1/2}$), the fully developed velocity profile given by Kaviany [10] is

$$g_m(z) = \Gamma_1 - \Gamma_2(e^{\beta[(z/h)-1]} + e^{-\beta(z/h)}),$$

where

$$\Gamma_1 = \frac{(1-e^{-2\beta})}{[1-e^{-2\beta}-2(1-e^{-\beta})^2\beta^{-1}]},$$

$$\Gamma_2 = \frac{(1-e^{-\beta})}{[1-e^{-2\beta}-2(1-e^{-\beta})^2\beta^{-1}]},$$

and $\beta = (H^2\phi/Da)^{1/2}$. So, the shape factor terms for the porous region can be written as

$$F^{(2)}_m = \Gamma_1 + \Gamma_2^2\left[2e^{-\beta} - \frac{(1-e^{-2\beta})}{\beta}\right]$$

$$\text{and} \quad f_m = \beta\Gamma_2(e^{-\beta}-1). \tag{14}$$

TOTAL PRESSURE DROP

Now that the mathematical model is completely defined, attention is directed towards the task of developing an equation capable of predicting the total pressure drop experience by the fluid across the cold plate, defined as $\Delta P/S = (\bar{P}_{in} - \bar{P}_{out})/S$.

An estimate of $\Delta P/S$ can be obtained considering the relative porous volume ε of the enclosure, defined as the ratio of the volume occupied by the porous layer to the total volume of the enclosure. With the porous layer covering the entire width of the enclosure, from $X = 0$ to $X = R$, and with S_m as the depth of the porous layer, the relative porous volume is $\varepsilon = RS_m/RS = S_m/S$. The determination of $\Delta P/S$ follows as a function of the pressure drop through the nonporous region, $\Delta P_f/S_f$, and the pressure drop through the porous region, $\Delta P_m/S_m$

$$\frac{\Delta P}{S} \sim \left(\frac{\Delta P_f}{S_f}\right)(1-\varepsilon) + \left(\frac{\Delta P_m}{S_m}\right)\varepsilon. \tag{15}$$

Nonporous and porous saturated pressure drops are obtained from scaling the continuity and momentum equations (10) and (11), considering each region separately (for details on scaling procedure refer to Nield and Bejan [9] and Bejan [11]). Within the nonporous region the result is

$$\frac{\Delta P_f}{S_f} \sim \frac{F^{(2)}_f}{R^2 S_f} + \frac{1}{RRe}\left(\frac{1}{S_f^2} - \frac{2f_f}{H^2}\right). \tag{16}$$

The last three terms of equation (16) are, respectively, convective inertia, viscous diffusion and surface viscous drag scales. Within the fluid saturated porous region, the scaling results in

$$\frac{\Delta P_m}{S_m} \sim \frac{F^{(2)}_m}{R^2\phi S_m} + \frac{\phi}{RRe}\left(\frac{J}{S_m^2} - \frac{J2f_m}{H^2} + \frac{1}{Da}\right) + \frac{\phi c_F}{R^2 Da^{1/2}} F^{(2)}_m, \tag{17}$$

where the last two terms of equation (17) are the scales of Darcy and Forchheimer terms.

Now, the nondimensional global pressure drop estimate can be obtained by combining equations (16) and (17) with equation (15),

$$\frac{\Delta P}{S} \sim \left(\frac{F^{(2)}_f}{RS_f} + \frac{1}{Re}\left(\frac{1}{S_f^2} - \frac{2f_f}{H^2}\right)\right)\frac{(1-\varepsilon)}{R} + \left(\frac{F^{(2)}_m}{R\phi S_m} + \frac{\phi}{Re}\left(\frac{J}{S_m^2} - \frac{J2f_m}{H^2} + \frac{1}{Da}\right) + \frac{\phi c_F}{RDa^{1/2}} F^{(2)}_m\right)\frac{\varepsilon}{R}. \tag{18}$$

Equation (18) is a useful tool as it identifies the nondimensional parameters that can influence the global pressure drop across the cold plate. It also anticipates the functional relationship between these parameters and the global pressure drop.

EFFECTIVE DARCY NUMBER

The re-dimensionalization process (reduction to a two-dimensional problem), from equation (2) to equation (11), transforms the term expressing the z-wise viscous diffusion of horizontal momentum into a Darcy-like term. Considering the coefficient multiplying the linear velocity term of equation (11), an effective Darcy number, Da^*, can be expressed as

$$\frac{1}{Da^*} = \left(-\frac{J2f_{f,m}}{H^2 F^{(2)}_{f,m}} + \frac{1}{F^{(2)}_m Da}\right), \tag{19}$$

where the groups within parentheses are the horizontal viscous diffusion coefficient and the original (porous medium) Darcy term coefficient, respectively. So, the boundary (viscous) effect of closely spaced top and bottom surfaces can be interpreted as a *volumetric viscous drag effect* within both, nonporous and

porous, regions. Noting that $f_{f,m}$ is always negative, the re-dimensionalization affects the flow decreasing the effective Darcy number (or decreasing the effective permeability) of the porous region.

Also noteworthy from equation (19) is that the original Darcy term coefficient within a porous region becomes negligible compared with the surface viscous drag coefficient when

$$Da \gg \frac{H^2}{-J2f_m}. \tag{20}$$

Moreover, from scaling equation (11), the form drag effect (Forchheimer term) is smaller than the viscous drag effect (Darcy term) within a porous region when

$$Da < \left(\frac{R}{F_m^{(2)} c_F Re}\right)^2. \tag{21}$$

Equations (20) and (21) reveal a very interesting and useful result: whenever they are satisfied, the existence of a permeable layer can be neglected from a hydraulic point-of-view. In this case, the entire enclosure can be modeled as a fluid region, simplifying the analysis considerably.

CONVECTIVE INERTIA LIMIT

There might be circumstances under which the viscous drag effect imposed by the z-plane surfaces predominates so as to make the convective inertia effect negligible. It is useful to appreciate under which conditions this happens, because if the convective inertia term becomes negligible it can be removed from the momentum equation. The equation then becomes linear within a nonporous region, which is very advantageous from a numerical point-of-view.

It is easy to verify from equation (16) that the convective inertia term becomes relevant only when

$$Re > \frac{R}{F_f^{(2)}}\left(\frac{1}{S_f} - \frac{2f_f S_f}{H^2}\right), \tag{22}$$

within a nonporous region, and when

$$Re > \frac{R\phi^2}{F_m^{(2)}}\left(\frac{J}{S_m} - \frac{J2f_m S_m}{H^2} + \frac{S_m}{Da}\right) \quad \text{and} \quad S_m < \frac{Da^{1/2}}{\phi^2 c_F}, \tag{23}$$

within a permeable region [from equation (17)]. Notice that the Reynolds constraint of equation (23) predominates over the porous region depth (S_m) constraint as long as the Darcy effect overcomes the Forchheimer effect, or in other words, whenever equation (21) is satisfied.

PHYSICAL CONFIGURATION

A typical cold-plate for a phased-array radar system consists of an enclosure measuring 0.5 m (width, r) by 0.15 m (depth, s) by 0.001 m (height, h). Inlet and outlet ports measure 0.025 m (e). In nondimensional form, the enclosure is 20 units long (R) by six units deep (S), with inlet and outlet one unit deep (E). The nondimensional height is $H = 0.04$. The electronic modules are approximately 0.075 m deep, therefore, the heating region is centered in the y-direction, being three nondimensional units deep.

The porous medium region is also centered in the y-direction, but it extends beyond the heating region with four units deep [see Fig. 1, (C)], aligned with inlet and outlet ports. The properties of the porous layer are porosity equal to 0.4 and permeability equal to 6.45×10^{-10} m^2, leading to $Da = 10^{-6}$ and $c_F = 1.75(150\phi^3)^{1/2} = 0.565$ (from Ergun [12] model with equivalent particle diameter of 7.4×10^{-4} m, representative of the mean diameter of the solid interconnections that form the metallic foam). These values of ϕ, K and c_F are consistent with values obtained experimentally from flow tests of some porous samples (Antohe *et al.* [13]). For this particular porous medium, the porous shape factors obtained from equation (14) are $F_m^{(2)} = 1.03924$ and $f_m = -27.47$. The flow Reynolds number is varied from 10 to 10^4.

A typical inlet coolant temperature is 25°C, and the total heat flux dissipated by the electronics is 7 kW m^{-2}. Three coolants are considered for the numerical simulations, namely air, water and polyalphaolefin (PAO—a synthetic oil used for cooling military avionics). Table 1 presents the thermal conductivity of each coolant and the corresponding Pr_m, considering an upper-bound value of the effective thermal conductivity, $k_m = \phi k + (1-\phi)k_s$ [15], where k and k_s are the fluid and solid-matrix thermal conductivities, respectively. Table 1 also presents the modified Prandtl number, Pr_{mH}, obtained using the phase-symmetry model recently proposed by Hsu *et al.* [16]. As it can be seen, the Pr_m values differ at most by a factor of two. The numerical nondimensional results are very sensitive to this variation. For instance, considering PAO and $Re = 10^4$, the maximum dimensionless temperature within the enclosure varies from $\theta_{max} = 46.29$ using $Pr_m = 0.1$, to $\theta_{maxH} = 26.46$ using $Pr_{mH} = 0.175$. However, the dimensional maximum temperature increase is insensitive to this variation: considering the same fluid (that is, same ϕc_p and ν), heat flux q'' and height h, the ratio of the dimensional maximum temperature increase using k_m to the dimensional maximum temperature increase using k_{mH} is

$$\frac{(T_{max} - T_{in})}{(T_{max} - T_{in})_H} = \left(\frac{Pr_m}{Pr_{mH}}\right)\frac{\theta_{max}}{\theta_{maxH}}, \tag{24}$$

where $Pr_m/Pr_{mH} = 0.571$ and $\theta_{max}/\theta_{maxH} = 1.749$. Therefore, the variation in Pr_m value has a negligible effect on the dimensional results. Notice from Table 1, using either the upper value model or the model by Hsu *et al.*, that the porous modified thermal conductivity is much higher than the fluid thermal con-

Table 1. Coolant and saturated porous medium properties: fluid thermal conductivity, k, and Prandtl number, Pr, effective thermal conductivity of porous medium, k_m [15] and k_{mH} [16], corresponding porous-modified Prandtl numbers, Pr_m, Pr_{mH}, fluid kinematic viscosity, ν, and thermal diffusivity, α

Coolant	k	Pr	k_m	Pr_m	k_{mH}	Pr_{mH}	ν	α
Air	2.5×10^{-2}	0.72	98.41	2×10^{-4}	50	3.5×10^{-4}	2.0×10^{-4}	2.06×10^{-5}
Water	6×10^{-1}	7	98.64	5×10^{-2}	42	10^{-1}	9.9×10^{-7}	1.42×10^{-7}
POA	1.45×10^{-1}	70	98.46	10^{-1}	58	1.75×10^{-1}	7.9×10^{-6}	1.13×10^{-7}

Notes: (1) all properties at 25°C; thermal conductivity in W m^{-1} K^{-1}, viscosity and thermal diffusivity in m^2 s^{-1}; (2) air and water properties from Bejan [11]; (3) PAO properties from Chevron [14]; (3) thermal conductivity of aluminum porous layer is approximately equal to 170 W m^{-1} K^{-1} and the thermal diffusivity is equal to 6.7×10^{-5} m^2 s^{-1}.

ductivity. Therefore, it is the latter that effectively controls the thermal diffusion process within the enclosure.

Equations (10)–(12), and shape parameters listed in equations (13) and (14), are solved using the finite volume method with SIMPLE algorithm [17] and QUICK scheme [18]. Discretized equations are solved with the efficient Tri-Diagonal-Matrix algorithm using an implicit alternating-direction Gauss–Seidel iterative method. The present code is a modified version (upgraded) of the one validated against experimental results by Lage *et al.* [19] simulating indoor pollutant transport through a ventilated enclosure.

Convergence criteria are: relative norm of pressure gradient being smaller than 10^{-6} for flow convergence, and relative norm of volume averaged temperature being smaller than 10^{-5} for energy equation convergence. After performing extensive grid accuracy tests, it is observed that a nonuniform (with grid lines clustered near solid interfaces and near nonporous–porous interfaces) 110 by 70 grid is sufficient to guarantee a three percent or smaller discrepancy with results obtained with a 160 by 100 grid.

The accuracy of the numerical simulations is also checked by performing a global energy balance within the enclosure. It is easy to show that for convection dominated heat transfer, the averaged nondimensional outlet fluid temperature has to satisfy

$$\bar{\theta}_{out} = \frac{RS_h}{H^2 RePr_m}, \tag{25}$$

where S_h is the nondimensional depth of the heating section. All results (excluding upstream diffusion phenomenon as detailed later on) satisfy this global balance within 0.01%.

RESULTS AND DISCUSSION

With the configuration described in the previous section, some important physical insight can now be obtained from the theoretical analysis. For instance, equation (20) indicates that the Darcy term is comparable with the surface viscous drag term because $\phi H^2/(-2f_m)$ is equal to 1.2×10^{-5}. Equation (21) predicts that the Forchheimer effect is negligible as long as $Da < 1160/Re^2$. For $Da = 10^{-6}$ this is true if $Re < 3.4\times10^4$.

The convective inertia effect is relevant within a fluid region, according with equation (22) with $S_f = 2$, when $Re > 3.75\times10^5$, a value that is beyond the Reynolds number range used here. Within the porous region, the convective inertia effect is relevant only when $Re > 1.23\times10^7$ and $S_m < 1\times10^{-2}$, from equation (23). None of these conditions are met in the present configuration (see that $S_m = 4$). Therefore, it seems as if the predominant hydraulic effects of this cold plate are the surface viscous effect and the Darcy effect.

Equation (18), with $\varepsilon = S_m/S = 4/6$, establishes that the equivalent global nondimensional pressure drop across the cold plate with porous layer is

$$\frac{\Delta P}{S} \sim \frac{1.46\times10^4}{Re} + 0.393. \tag{26}$$

For comparison purposes, a nonporous enclosure (without porous layer) is also considered. The predicted nondimensional pressure drop, from equation (18) with $\varepsilon = 0$, is

$$\frac{\Delta P}{S} \sim \frac{3.75\times10^2}{Re} + 5\times10^{-4}. \tag{27}$$

The accuracy of these theoretical hydraulic predictions is checked against the numerical results obtained by solving the general equations. The numerical hydraulic results (continuous lines) are presented in Fig. 2, side by side with the predicted theoretical values (dashed lines) listed in equations (26) and (27). The porous layer (thick line) and nonporous (thin line) numerical results can be fitted, respectively, by: $\Delta P/S = 0.6 + (2.38\times10^4/Re)$ and $\Delta P/S = 5.65\times10^2/Re$. Therefore, the theoretical pressure drop functional dependence on the Reynolds number, predicted by equations (26) and (27), is confirmed by the numerical results.

The theoretical and numerical results for nonporous and porous configurations deviate from the numerical results by a constant factor of order one, as expected in scale analysis. The anticipated usefulness of equation (18), that of predicting the correct order of magnitude of the total pressure drop, is confirmed.

The low theoretical estimate of pressure drop might be related to the fluid travel length from inlet to outlet,

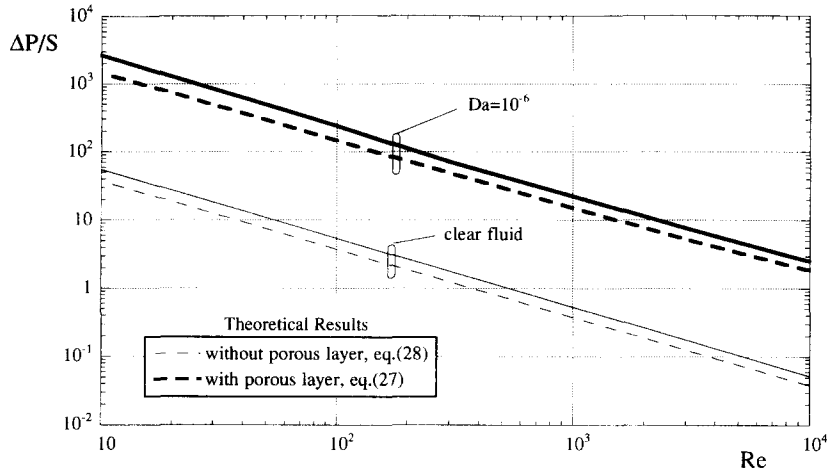

Fig. 2. Nondimensional pressure drop across a cold plate: comparison of theoretical estimates (dashed lines) and numerical results (continuous lines).

assumed in the scale analysis to be equal to the depth of the enclosure. It will be shown later on, from streamline mapping of the flow through the cold plate, that the fluid travel length is larger than the depth of the cavity, and by consequence the pressure drop should also be higher.

Notice, from Fig. 2, that the numerical nondimensional pressure drop with the porous layer in place is approximately 40 times higher than without the porous layer, throughout the Reynolds number range investigated here.

Equally spaced streamline distributions, for $Re = 3000$ [frames (a) and (b)] and $Re = 30$ [frames (c) and (d)] are shown in Fig. 3. The coolant flows from top left (inlet) to bottom right (outlet). Some nondimensional streamfunction values are indicated in the figure. Notice how the flow becomes aligned with the depth of the enclosure when the porous layer is in place [frames (a) and (c)]. Also, observe in frames (a) and (c), along the heating region, the increasing spacing between streamlines from inlet surface towards the mid-width of the enclosure, and the decreasing spacing from mid-width towards outlet surface. This indicates a faster flow near the inlet and outlet surfaces, a consequence of the slightly skewed flow. There is only a very small difference on the streamline distribution of the configuration without the porous layer [frames (b) and (d)] as the Reynolds number is reduced: the lowest flow streamline [see arrow in frames (b) and (d)] extends itself from the inlet port a little more along the width of the enclosure for high Re. The fact that the streamline distribution is basically unchanged as the Reynolds number increases from 30 to 3000 in both configurations is an indication that inertia effects are indeed negligible within this range.

The nondimensional hydraulic results are independent of the fluid (the only fluid related parameter governing the mass and momentum balance, equations (10) and (11), is the Reynolds number). This is not the case of the nondimensional temperature values, as the energy equation (12) depends on the Prandtl number that depends on the coolant. In Fig. 4, equally spaced isotherms for $Pr = 70$ and $Pr_m = 0.1$ (characteristic of PAO flowing through an aluminum porous matrix) are presented. The top two frames for $Re = 3000$ indicate that the porous layer [frame (a)] induces a much more uniform temperature along the width of the enclosure within the heating region than the case without the porous layer [frame (b)]. The inlet plenum is maintained at almost uniform temperature (close to the inlet temperature, $\theta = 0$) due to the convection effect and due to the relatively low heat diffusion of PAO (high Pr).

The equally spaced isotherms for clear enclosure configuration (no porous layer) and $Re = 3000$, frame (b), resemble those of a viscous dominated flow. Notice how the location of maximum temperature (indicated with a '+' symbol), at the outlet plenum, moves towards the outlet of the enclosure when compared with frame (a). The isotherms for $Re = 30$ and no porous layer [frame (d)] are basically unchanged, except that the isotherms along the inlet surface (see arrows near left surface) deepens less towards the outlet plenum than those for the case $Re = 3000$ [frame (b)].

A peculiar isotherm distribution is that with porous layer configuration and $Re = 30$, frame (c). The isotherms are also equally spaced, but the isotherm closest to the inlet plenum is already at 58% of the maximum temperature within the enclosure ($\theta_{max} = 12.5 \times 10^3$). This fact indicates the existence of a very large temperature gradient within the inlet plenum. Although less uniform that the isotherms of the case $Re = 3000$, the actual temperature variation within the heating region is relatively small, as they vary by only 42% of the maximum temperature value. This peculiar behavior is also present when water is used as coolant, Fig. 5 frame (c). In this case, the isotherm closest to the inlet plenum is at 54% of the

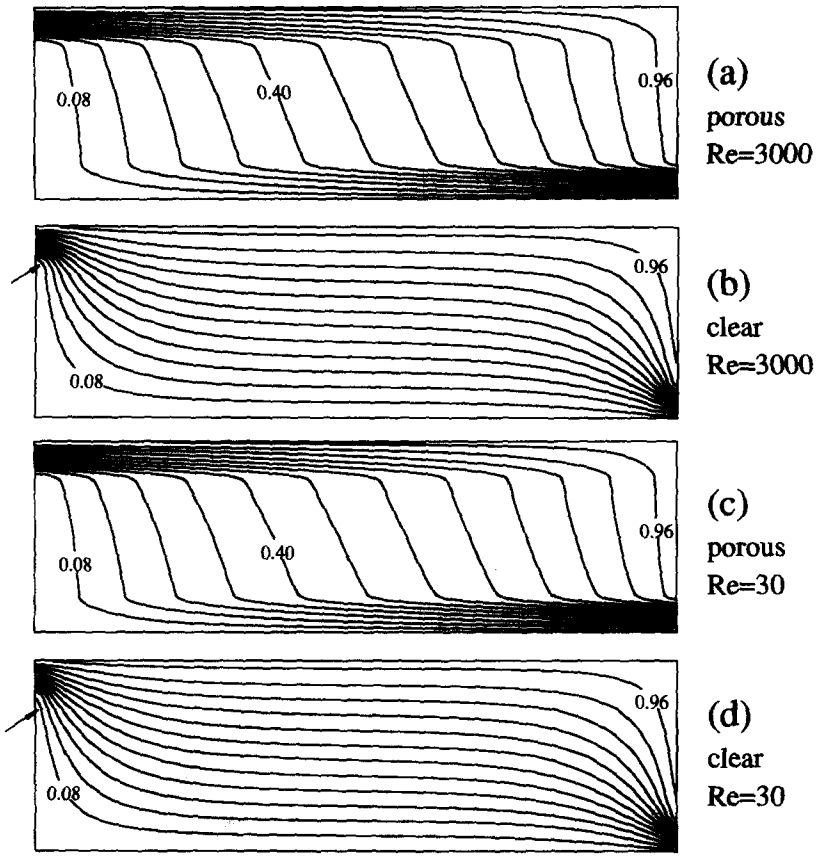

Fig. 3. Equally spaced streamlines for a configuration with a porous layer (porous) and a configuration without a porous layer (clear).

maximum temperature. The isotherms for water (Fig. 5) and $Re = 3000$, with porous layer [frame (a)] and without porous layer [frame (b)] are similar to those for PAO shown in Fig. 4. For $Re = 30$ and no porous layer [frame (d)] the isotherms are more spread out than those of PAO. Recall from Table 1 that the Prandtl number ratio Pr/Pr_m drops from 700 (PAO) to 140 (water), therefore the heterogeneity of the system is reduced as the coolant heat diffusion is increased in relation to that of the porous region. Another peculiarity is that the max-θ location shifts from near the center to near the exit of the enclosure as Re decreases (Figs. 4 and 5). This is caused by the predominance of diffusive transport at low Re and the particular inlet—isothermal—boundary condition.

Figure 6 (top) presents the overall thermal effect in terms of maximum nondimensional temperature within the enclosure for all three coolants, with and without the porous layer. This is a fundamental engineering design result as it indicates the ability of the system to maintain the temperature of the electronics below a certain level. Notice that if one defines a heat transfer coefficient as equal to $(T' - T_{in})/q''$ then the nondimensional temperature definition [second paragraph following equation (9)] is equivalent to the definition of a Nusselt number corresponding to this heat transfer coefficient.

As seen in Fig. 6, PAO is the coolant that provides the lowest nondimensional maximum temperature, followed by water and air, in both configurations. The thin line curves, for configuration without the porous layer, follow the Pr trend as the increase in θ_{max} is almost directly proportional to the increase in Pr. The same is true for the maximum temperature of the porous layer case (thick lines), proportional to Pr_m. By the way, Fig. 6 (top) indicates that is it the lowest Prandtl number within the system that dominates the maximum nondimensional temperature value.

Figure 6 (top) seems to indicate also that an enclosure without a porous layer is preferable to one with a porous layer, as lower θ_{max} values are obtained for the same coolant at same Re. In Fig. 6 (bottom), the maximum transversal temperature difference (maximum difference between two temperatures along the width—x-direction—of the enclosure) within the heating region, $\Delta\theta_{max}$, is plotted vs Re. Notice that the maximum temperature difference increases with decreasing Prandtl number, as in Fig. 6 (top). Also in this case, the thermal performance of the system seems to deteriorate with the porous layer in place. This apparent contradiction is resolved considering the dimensional temperatures as explained next.

In Fig. 7, the nondimensional temperature results have been dimensionalized using the property values

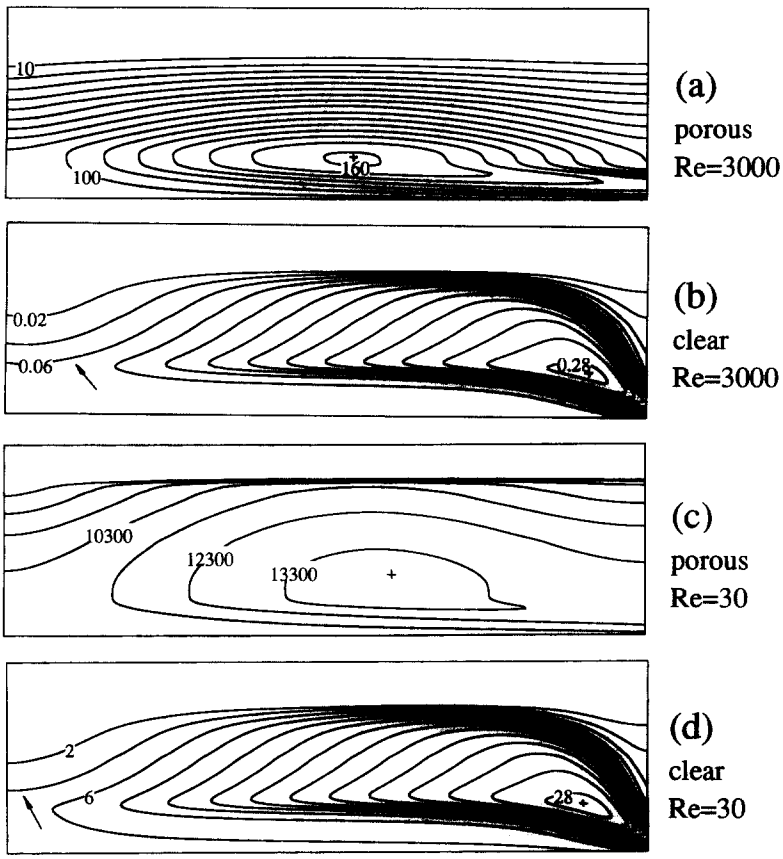

Fig. 4. Isotherm distribution of PAO: $Pr = 70$, $Pr_m = 10^{-1}$ ('+' indicates location of maximum temperature).

listed in Table 1 (k and k_m), assuming cold plate height of 0.001 m, inlet coolant temperature of 25°C, and heat dissipation rate of 7 kW m^{-2}, typical of phased-array radar systems. Dimensional maximum temperature in degrees Celsius (related to the inlet coolant temperature) is plotted in the top graph, and the dimensional maximum transversal temperature difference across the modules (within the heating region, along the x-direction) in degrees Celsius is plotted in the bottom graph.

Although having a smaller thermal conductivity than water, PAO provides the best cooling of all three fluids, that is, it provides the lowest maximum temperature at the heating region for the same Reynolds number. It is very important to stress that the same Reynolds number of fluids with such distinct viscosities (see Table 1) translates into different inlet velocities. In fact, the volumetric flow rate of PAO will have to be roughly eight times that of water for the same Reynolds number.

Within the Reynolds range presented in Fig. 7 (top), air is unable to provide acceptable cold plate temperature. Linear extrapolation of the air curves anticipates that the flow Reynolds number should be higher than 10^6 for a maximum temperature difference lower than 100°C.

The no porous layer configuration (thin lines) leads to maximum temperature (Fig. 7, top) of about 120, 70 and 40% higher than the maximum temperature attained with the porous layer for air, water, and PAO, respectively. Also, the temperature uniformity is improved with the porous layer, as indicated by the bottom graph of Fig. 7. The impact is more evident for air where the maximum temperature difference drops by more than 40 times with the porous layer. For water, the decrease in maximum temperature difference is of about eight times, and for PAO the decrease is of about six times. The variation from coolant to coolant is related to the improved thermal conductivity achieved by placing the porous layer within the enclosure. The level of improvement is reflected by the ratio of k to k_m, from Table 1, equal to 2.54×10^{-4} (air), 6.08×10^{-3} (water), and 1.47×10^{-3} (PAO). Therefore, the thermal impact of placing the aluminum porous layer within the enclosure is greater when very low conductivity coolant is used.

LIMITATIONS

The separation of variables, as, for example, $u = u'(x, y)g(z)$, when the flow region is a sequence of nonporous–porous–nonporous... regions requires the assumption that all hydrodynamic development lengths are negligibly small.

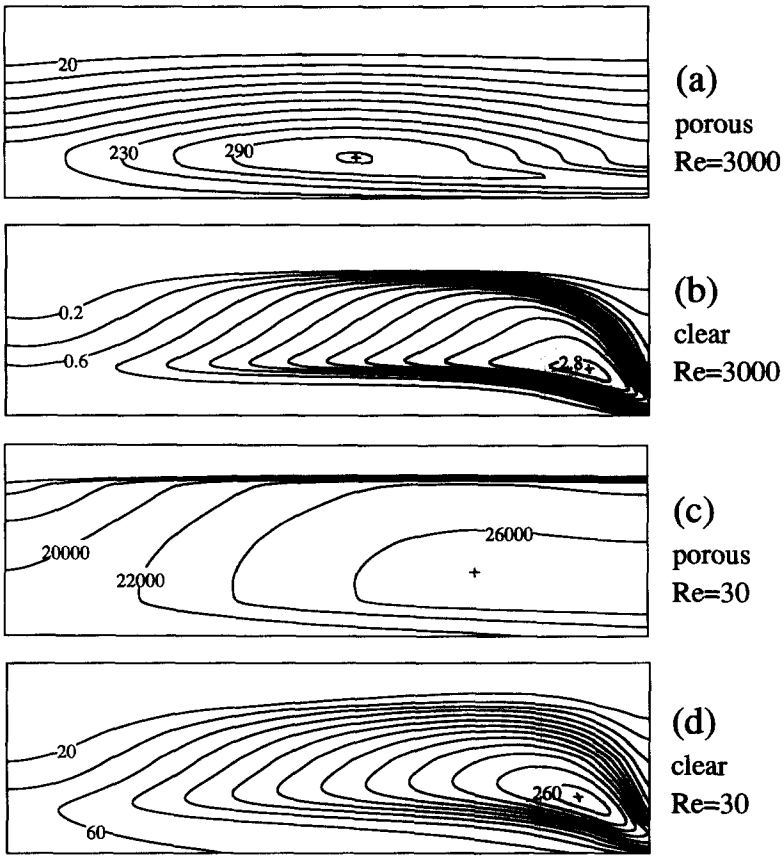

Fig. 5. Isotherms distribution of water: $Pr = 7$, $Pr_m = 5 \times 10^{-2}$ ('+' indicates location of maximum temperature).

For transition from the nonporous to porous region, the assumption is accurate as long as the Darcy number is small: the developing length in a low permeability porous region is predicted as $x_m \sim hDa^{1/2}$ [9], in the present case $x_m \sim 10^{-6}$ m, shorter than the porous layer depth of 0.1 m.

The transition from porous to clear region is more subtle. For nonporous flow through parallel plates, with uniform incoming flow, the entrance length is predicted as $x_f = 0.0065hReH$ [20], where Re is based on e. So, for $h = 0.001$ m, $Re = 10^4$, and $H = 0.04$, the developing length is of the order of 0.0026 m which is about 10 times smaller than the shortest plenum depth assumed here equal to 0.025 m. Since the flow coming out of a low permeability porous region is not uniform (distorted due to Brinkman effect) the development length is expected to be even shorter (this effect might be negligible if porosity variation near the surface is included in the analysis). Flow with $Re < 10^4$ will present an even shorter developing length.

Noticeable in Fig. 6 are the dashed-extensions at low Reynolds number for the porous layer cases of air and water as coolant. These curve sections are drawn with dashed lines as an indication that the convective limit of the numerical simulations has been reached. These results, although mathematically and numerically correct, are not realistic from a physics perspective. Recall, with reference to the PAO [Fig. 4(c)] and water [Fig. 5(c)] isotherms, that a very large temperature gradient builds-up within the inlet plenum at low Reynolds numbers. It so happens that this large temperature gradient leads to a heat flow through the inlet port in an opposite direction to the incoming fluid. As the Prandtl number decreases from PAO to water to air, heat diffusion becomes predominant. As the inlet temperature is maintained constant, heat starts to *leak* from the heating section through the incoming fluid (that is why the maximum temperature decreases as Re is reduced, Fig. 6—top). When this diffusion transport surpasses the convective transport, the convective limit is reached as indicated by the dashed lines. The results are no longer realistic since the inlet temperature would change as affected by the upstream heat flow. This phenomenon is emphasized in Fig. 8, where isotherms for the case of air (lowest Pr used here) as coolant are plotted. Frames (a) for porous layer and (b) for no porous layer are with $Re = 3000$. Frame (c) presents isotherms of nonporous configuration and $Re = 30$. The isotherm closest to the inlet plenum of frame (a) is equivalent to 85% of the maximum temperature. See in frame (c) that, with air as a coolant, the diffusion effect is predominant at $Re = 30$, even for con-

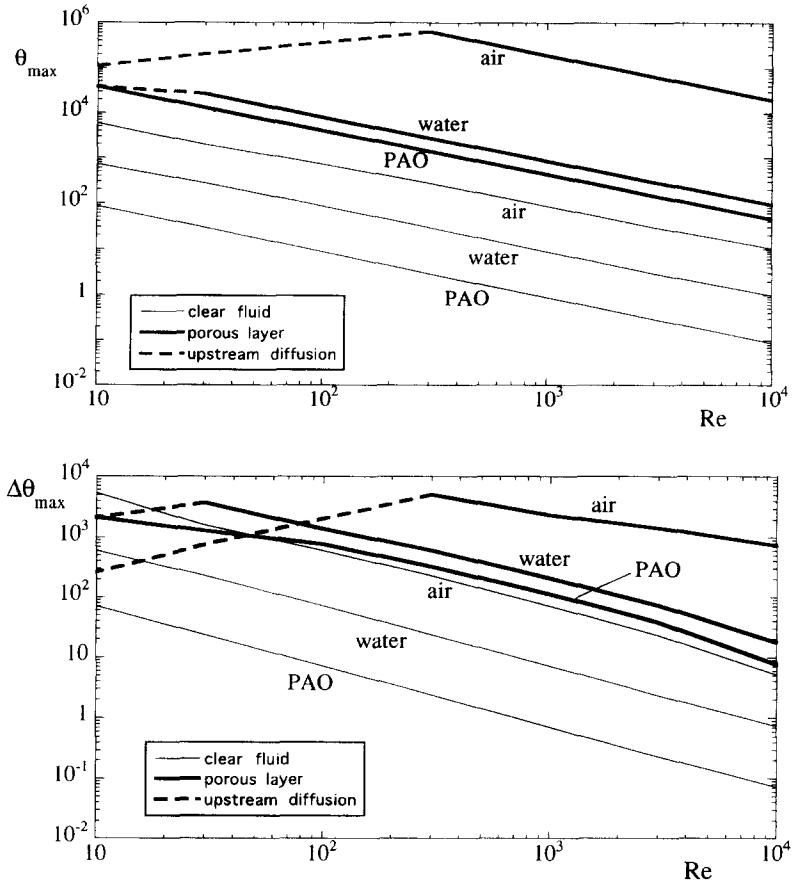

Fig. 6. Top: maximum nondimensional temperature within the cold plate for air, water and PAO vs Reynolds number. Bottom: maximum nondimensional transverse temperature difference (along the width of the enclosure) within the heating region, for air, water and PAO vs Reynolds number.

figuration without the porous layer (in all cases the isotherms are equally spaced).

The correctness of imposing a nondiffusion temperature boundary condition at the outlet of the enclosure is now discussed. The zero diffusion outlet boundary condition was shown by Lage *et al.* [19] to have negligible effect on the numerical simulation of ventilated two dimensional enclosures. The same conclusion has been reached recently by Safi and Loc [21] on their study of thermal stratification in a cavity with through flow. Presently, for Prandtl number larger than one when convection predominates, the diffusive outlet boundary condition effect becomes less pronounced. For $Pr = 0.72$ the maximum difference between averaged temperatures obtained with nondiffusive outlet boundary and with diffusive boundary and constant temperature $\theta_{out} = 0$, is less than 5%.

A final note is necessary regarding the thermal equilibrium assumption. This assumption is known to deteriorate for high Reynolds number and high Darcy number, depending on the solid matrix to fluid thermal diffusivity ratio. This dependence is not a simple one, as indicated in the work of Amiri and Vafai [22] considering a porous medium made of identical spherical particles, particle Reynolds number from 0 to 450, and Darcy number from 0 to 15×10^{-7} (see their Fig. 7). The solid matrix and fluids considered here present diffusivity ratio in the 1–700 range, the maximum Reynolds number of 10^4 translates into a particle-based *Re* of around 250, and *Da* is equal to 10^{-6}. Although Amiri and Vafai's qualitative mapping does not go beyond diffusivity ratio 25, it anticipates the thermal equilibrium assumption to be a reasonable approximation.

CONCLUSIONS

The single phase, forced convection cooling of a phased-array radar slat is studied theoretically and numerically. The cooling device is considered as a very thin enclosure with one inlet and one outlet. The thermo-hydraulic effects of placing an aluminum porous layer within the cooling enclosure is analyzed for three distinct coolants, namely air, water and PAO. Results are compared with the results of a clear (of porous material) device.

A two-dimensional flow model, valid for slender enclosures partially filled with a porous layer, considering the convective inertia effects, the viscous (Brinkman) effects, and the additional drag effects

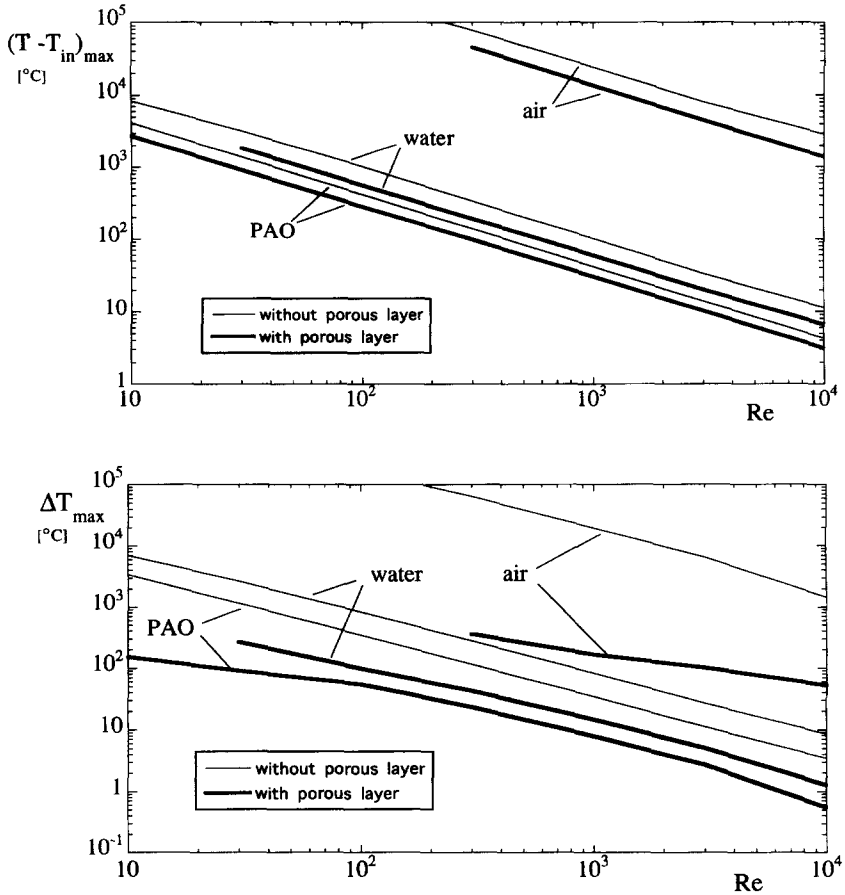

Fig. 7. Top: maximum dimensional temperature within the cold plate versus Reynolds number. Bottom: maximum dimensional transverse temperature difference within the heating region, for air, water, and PAO, versus Reynolds number (case study: k and k_m from Table 1, $h = 0.001$ m, $q'' = 7$ kW m^{-2}).

(viscous and form) within the permeable region, is obtained by integrating the three-dimensional equations along the spacing of the enclosure. The integration process leads to additional unknowns, called shape functions, obtained from the fully developed velocity profiles within each region. A simple closure for the problem is obtained by using known analytical solutions of velocity distribution valid for low permeability porous media.

Theoretical analyses provide limits within which the viscous drag effect predominates over the Darcy effect [equation (20)], the Darcy effect predominates over the Forchheimer effect [equation (21)], and the inertia effect is predominant within the nonporous region [equation (22)] and within the porous region [equation (23)]. These results are fundamental for at least one reason: they anticipate those configurations in which the nonlinear terms might be neglected, reducing considerably the computational effort necessary for simulating the transport phenomena.

A general theoretical expression for predicting the total pressure drop within the cooling enclosure is obtained by scaling the momentum equation. One must realize that the main benefit of a properly performed scale analysis is not a perfect quantitative matching between predicted and measured values, but the establishment of the relative (functional) importance of each parameter to influence the variations of the primary quantity of interest. The result, equation (18), provides an estimate of the total pressure drop across the enclosure, fundamental for preliminary design considerations. The Reynolds number functional estimate was confirmed by the numerical results.

Isolines present the main hydraulic and thermal features of the design considered here. They indicate that a high degree of flow uniformity is achieved along the width of the enclosure when a porous layer is in place. The penalty for the more uniform flow is an increase on the pressure drop from inlet to outlet of the enclosure, compared against an enclosure with no porous layer. The more uniform flow clearly reduces the temperature gradient along the width of the enclosure.

The efficiency of the cooling enclosure with porous layer is checked, for each coolant, against the efficiency of a clear enclosure. The results are presented in terms of maximum temperature within the enclosure and the maximum transversal temperature difference, within the heating zone. It is found that the aluminum porous layer always enhances the cool-

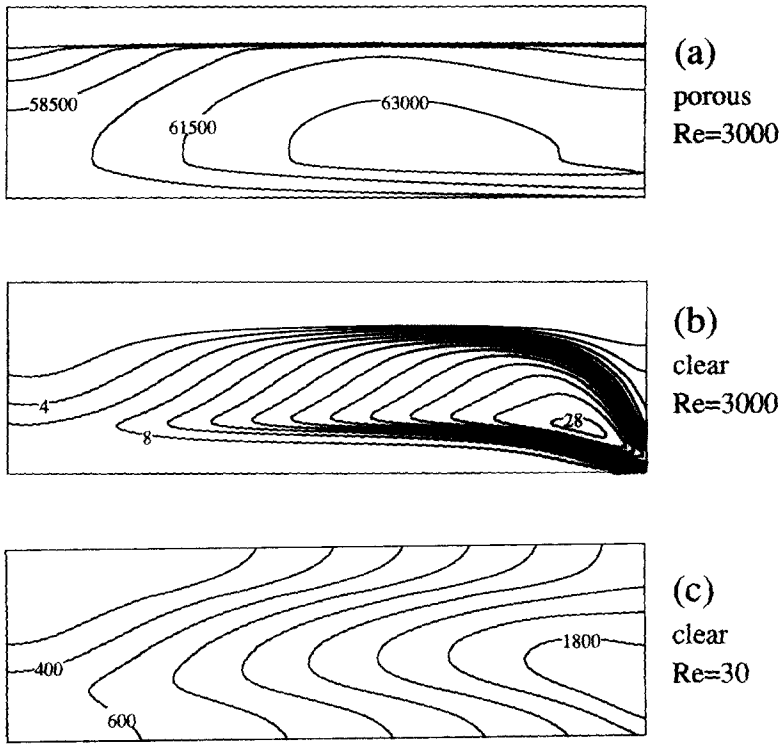

Fig. 8. Isotherm distribution of air: $Pr = 0.7$, $Pr_m = 2 \times 10^{-4}$.

ing of the slat in two respects: reducing the maximum temperature and reducing the maximum transversal temperature difference. The thermal impact is greater when low thermal conductivity coolant is used. Nevertheless, the worst case (for PAO) presents an improvement of 33% lower maximum temperature and 700% lower maximum transversal temperature difference.

Acknowledgements—Professor Lage is grateful for the financial support provided by Texas Instruments. Ms Weinert acknowledges with gratitude the Embrey Summer Research Scholarship from the School of Engineering and Applied Science of SMU. Part of this work was performed on a DEC Alpha/AXP 3000/600, running OSF 1.2, provided under a seed grant program agreement.

REFERENCES

1. I. Mudawar, P. E. Jimenez and R. E. Morgan, Immersion-cooled standard electronic clamshell module: a building block for future high-flux avionics systems. *J. Electron. Packaging* **116**, 116–125 (1994).
2. J. N. Walpole and L. J. Missaggia, Microchannel heat sinks for two-dimensional diode laser array. In *Surface Emitting Semiconductor Lasers and Arrays* (Edited by G. A. Evans and J. M. Hammer), Vol. 1. Academic Press, New York (1993).
3. X. F. Peng, B. X. Wang, G. P. Peterson and H. B. Ma, Experimental investigation of heat transfer in flat plates with rectangular microchannels, *Int. J. Heat Mass Transfer* **38**, 127–137 (1995).
4. P. C. Huang and K. Vafai, Analysis of forced convection enhancement in a channel using porous blocks, *J. Thermophys. Heat Transfer* **8**, 563–573 (1994).
5. A. Hadim, Forced convection in a porous channel with localized heat sources, *J. Heat Transfer* **116**, 465–472 (1994).
6. A. Hadim and A. Bethancourt, Numerical study of forced convection in a partially porous channel with discrete heat sources. *J. Electron. Packaging* **117**, 46–51 (1995).
7. R. C. Chu and R. E. Simons, Recent development of computer cooling technology. In *Transport Phenomena in Thermal Engineering* (Edited by J. S. Lee, S. H. Chung, and K. Y. Kim), Vol. 1, pp. 17–25. Begell House, New York (1993).
8. C. T. Hsu and P. Cheng, Thermal dispersion in a porous medium, *Int. J. Heat Mass Transfer* **33**, 1587–1597 (1990).
9. D. A. Nield and A. Bejan, *Convection in Porous Media*. Springer, New York (1992).
10. M. Kaviany, Laminar flow through a porous channel bounded by isothermal parallel plates, *Int. J. Heat Mass Transfer* **28**, 851–858 (1985).
11. A. Bejan, *Heat Transfer*. Wiley, New York (1993).
12. S. Ergun, Fluid flow through packed columns, *Chem. Engng Prog.* **48**, 89–94 (1952).
13. B. V. Antohe, J. L. Lage, D. C. Price, R. M. Weber, Experimental determination of permeability and inertia coefficients of mechanically compressed aluminum porous matrices, *J. Fluids Engng* (submitted).
14. Chevron, *Synfluid and Synthetic Fluids*. Physical Property Data, San Francisco, CA (1981).
15. G. K. Batchelor and R. W. O'Brien, Thermal or electrical conduction through granular material, *Proc. R. Soc. Lond.* **A355**, 313–333 (1977).
16. C. T. Hsu, P. Cheng and K. W. Wong, Modified Zehner–Schlunder models for stagnant thermal conductivity of porous media, *Int. J. Heat Mass Transfer* **37**, 2751–2759 (1994).
17. S. V. Patankar, *Numerical Heat Transfer and Fluid Flow*. Hemisphere, Washington DC (1980).
18. B. P. Leonard, A stable and accurate convective modeling procedure based on quadratic upstream interpolation, *Comput. Meth. Appl. Mech. Engng* **19**, 59–98 (1979).

19. J. L. Lage, A. Bejan and R. Anderson, Efficiency of transient contaminant removal from a slot ventilated enclosure, *Int. J. Heat Mass Transfer* **34**, 2603–2615 (1991).
20. E. M. Sparrow, Analysis of laminar forced convection heat transfer in the entrance region of flat rectangular ducts, NACA TN-3331 (1955).
21. M. J. Safi and T. P. Loc, Development of thermal stratification in a two-dimensional cavity : a numerical study, *Int. J. Heat Mass Transfer* **37**, 2017–2024 (1994).
22. A. Amiri and K. Vafai, Analysis of dispersion effects and non-thermal equilibrium non-Darcian, variable porosity incompressible flow through porous medium, *Int. J. Heat Mass Transfer* **37**, 939–954 (1994).